Correction of Magnetic Field Inhomogeneity Effects Using Conjugate Phase Reconstruction

Aggariyo Wanagiri

MSc Thesis in BioMedical Engineering

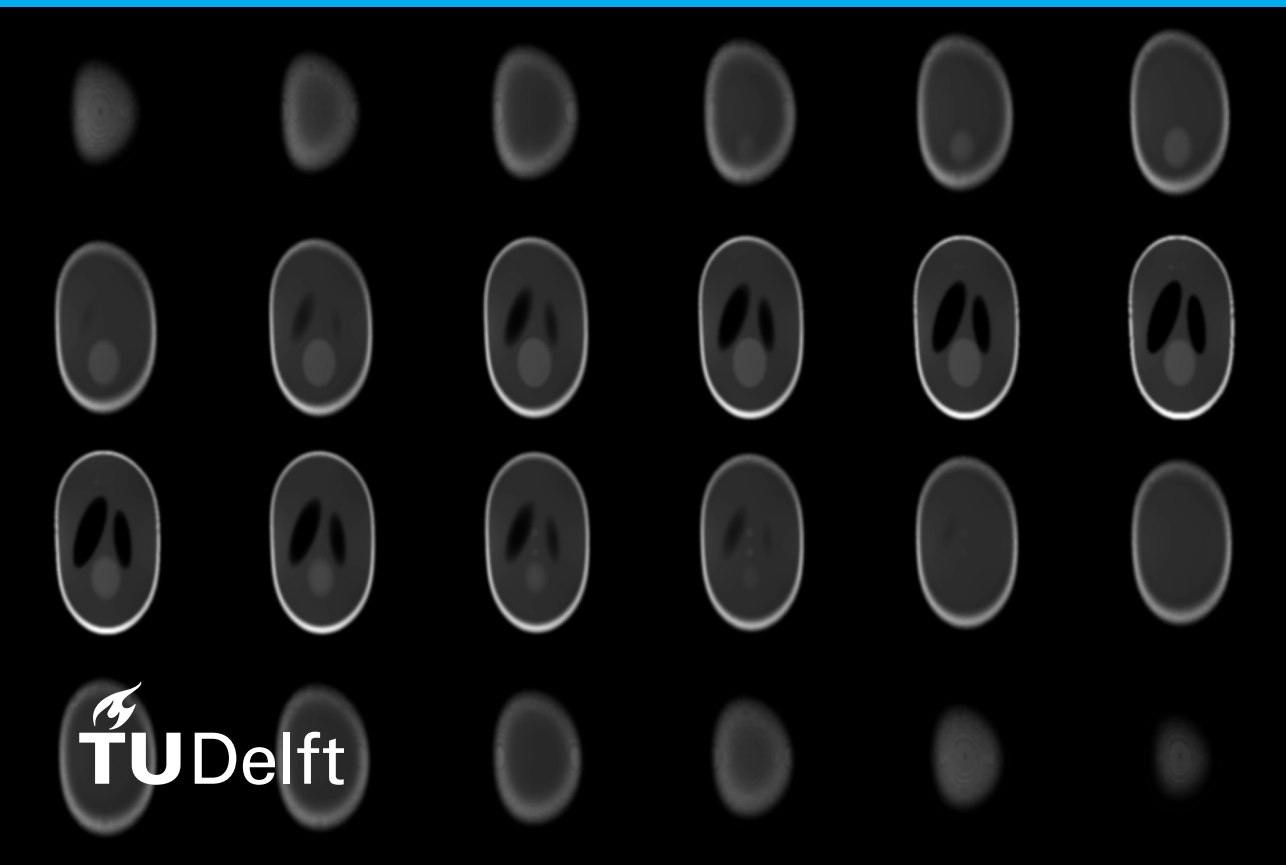

TU Delft

CORRECTION OF MAGNETIC FIELD INHOMOGENEITY EFFECTS USING CONJUGATE PHASE RECONSTRUCTION

by

Aggariyo WANAGIRI

to obtain the degree of
Master of Science
in Biomedical Engineering
at the Delft University of Technology

To be defended publicly on Tuesday May 31st, 2022 at 16:00

Student number:	5419883	
Project duration:	15 Nov 2021 - 31 May 2022	
Supervisor:	Dr. Ir. K. Koolstra	LUMC
	Dr. Ir. R.F. Remis	TU Delft

ABSTRACT

Low field magnetic resonance imaging (MRI) scanners provide a unique low-cost alternative to conventional MRI scanners. Nevertheless, low-field scanners come with drawbacks such as reduced signal-to-noise ratio and resolution, and also distorted images caused by magnetic field inhomogeneity and non-linear gradient fields. Despite this, it still provides a more accessible way to provide MRI in resource-limited areas. The main goal of this thesis is to develop an algorithm that can reconstruct 3D data from the low-field scanner efficiently and without distortion to the image. To do this, conjugate phase reconstruction (CPR) is employed, particularly frequency segmented reconstruction (Noll, 1991) and multifrequency interpolation (Man et al., 1997).

ACKNOWLEDGEMENTS

With this paper, I am closing a chapter in my life and looking forward to the opening of a new one. Living abroad was not always easy, but the friends I have made along the way have given me a sense of belonging in this world and I am very grateful to all of them.

Firstly, I would like to express my appreciation to Dr. Ir. R.F. Remis for teaching a really interesting class on MRI, and for introducing me to this project. He has been a good supervisor throughout the project who helped with a lot of the organisational aspects, and has provided clear explanations to the questions I have asked. I would also like to express my appreciation to my daily supervisor, Dr. Ir. K. Koolstra, to whom without, this project would not have been possible. Her work on the topic provided a solid basis for this paper, and she helped tackle the problems I encountered in the project.

Lastly, I would like to thank my parents for the opportunities they gave me, and also my brother for being there when I needed it. I also would like to thank my girlfriend Jeanne. Her support has been indispensable throughout this whole process, and has helped me through a lot of tough times.

Aggariyo Wanagiri
Den Haag, Netherlands
15th of May 2022

CONTENTS

1

INTRODUCTION

Currently, medical imaging has become an integral part of healthcare. Imaging modalities such as ultrasound, CT and MRI, are now widely used in hospitals throughout the world and have been useful in the diagnosis and treatment of many types of diseases. MRI specifically, is most well known for its ability to provide high contrast images of soft tissue. Most MRI scanners that are currently used have magnetic field strengths that range from 1.5T to 7T. While they are sometimes indispensable, they are not always available due to costs associated with acquiring and maintaining the machine. This chapter will cover a clinical application of MRI, which has lead to the development towards a low-cost alternative, low-field scanner.

1.1. HYDROCEPHALUS

Normally, cerebrospinal fluid (CSF) circulates through the brain and spine, and is then reabsorbed through the bloodstream. Hydrocephalus is a condition characterised by a build up of CSF inside ventricles within the brain. This causes the ventricles to swell and exert pressure inside the skull. Figure 1.1 shows an image of a brain affected by hydrocephalus. This condition occurs most often in children, and can lead to learning, or physical disabilities, and may eventually prove to be fatal (*Hydrocephalus Overview*, n.d.). Therefore, early diagnosis is important, and leads to a lower chance of long-term complications. In order to treat hydrocephalus, a shunt can be surgically inserted to divert the excess fluid into either the chest cavity or abdomen where the fluid will be absorbed (*Hydrocephalus Fact Sheet*, n.d.). Unfortunately, in developing countries, the condition is often left untreated. When head swelling becomes prominent, the brain tissue is undeveloped and surgery becomes rare and difficult (Borden et al., 1918). Hydrocephalus can be caused by genetic or environmental factors before birth, and is most prevalent in low- and middle-income countries (Dewan et al., 2019). It is currently the most common reason for brain surgery in children, and cases of infant hydrocephalus is estimated to effect as many as 225,000 children per year in sub-Saharan Africa (Dewan et al., 2019).

1

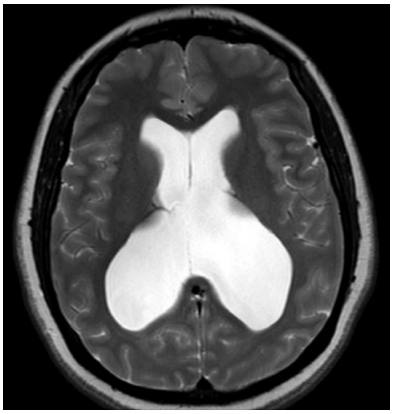

Figure 1.1: TSE T2 weighted image of a brain affected by hydrocephalus with a build up of fluid in the centre Dinçer and Özek, 2011.

There are multiple methods of diagnosis. Ultrasound is a low-risk method but is only effective at 14-16 weeks when the skull is thin (Paladini et al., 2007). CT and MRI are more expensive alternatives, but provide a clearer image. While CT is often used, multiple follow-up scans exert a radiation burden towards the patient. MRI does not use radiation and therefore contains less risks. Nevertheless, it is not always available, especially due to the high costs associated with acquiring and maintaining the system.

1.2. LOW-FIELD MRI

Current MRI scanners used in hospitals range from 1.5T to 7T, and it is necessary to house the scanner in an electromagnetically shielded room. This is done to prevent the scanner from disrupting nearby medical devices, and also to protect the scanner from outside interference. A shielded room can cost as much as $100,000. Moreover, conventional 1.5T scanners can cost upwards of $800,000 (Wald et al., 2020). Overall, the high costs of MRI scanners have discouraged the use of this technology especially in low and lower-middle income countries (WorldHealthOrganization, n.d.). Nevertheless, hydrocephalus and other types of brain disorders, create a demand and need for an affordable alternative. Low-field MRI scanners aims to provide this. Although a lower magnetic field results in an image with lower resolution, it should still be sufficient for use in the early diagnosis of brain disorders like hydrocephalus.

Normal MRI scanners use a large superconducting magnet and a cooling system to continuously generate a strong magnetic field. Currently, a 50mT scanner is being developed in the Leiden University Medical Center (LUMC) which uses a Halbach array of permanent magnets (O'Reilly et al., 2021), shown in Figure 1.2. This significantly reduces the manufacturing and maintenance costs, and also the size of the scanner. Moreover, the entire setup is placed inside a Faraday cage made of aluminium. This way, a shielded room is not needed for the operation of the scanner. Nevertheless, low-field scanners come with drawbacks such as reduced SNR, resolution, and also image distortion.

Figure 1.2: Low-field MRI scanner currently being developed in LUMC by O'Reilly et al., 2021.

1.3. THESIS OBJECTIVE

Currently, the low-field scanner experiences magnetic field inhomogeneity and a non-linear gradient field. Normal reconstruction techniques using FFT in the presence of field disturbances result in a spatial distortion in the resulting images. The main goal of this thesis is to develop an algorithm that can reconstruct 3D data from the low-field scanner efficiently and without distortion to the image. To do this, conjugate phase reconstruction is employed, using papers by Koolstra et al., 2021, Man et al., 1997, and Noll, 1991 as a basis.

Firstly, the MRI signal model will be derived by using the Bloch equation. Then, the theory behind conjugate phase reconstruction will be explained, followed by subsets of the method, frequency segmented reconstruction and multifrequency interpolation. Subsequently, the reconstruction methods will be tested on two Shepp-Logan phantoms, the first is distorted by B_0 field inhomogeneity, while the second is distorted by both B_0 field inhomogeneity and non-linear gradient fields. The results of each method will be compared by calculating the residual norm error, and the speed of each method will be discussed as well. Finally, the chosen reconstruction method will be tested on in vivo datasets obtained from the low-field scanner.

2

SIGNAL MODEL

In this chapter, we look at the mathematics behind MRI. This is done by first explaining the nuclear magnetic resonance (NMR) phenomenon, which MRI relies upon to generate images. Followed by the Bloch equation, which is fundamental to describing the nuclear magnetization as a function of time at each point in the system. The Bloch equation in this chapter outlines lecture notes given in the course "Advanced Magnetic Resonance Imaging" in TU Delft (Remis, n.d.).

2.1. NUCLEAR MAGNETIC RESONANCE

Nuclear magnetic resonance is a phenomenon that is fundamental to creating images in MRI. As the name suggests, this phenomenon consists of three parts. The first part concerns the nuclei of atoms, particularly nuclei that have an odd atomic number or an odd mass number. These nuclei possesses an angular momentum $\boldsymbol{\phi}$, otherwise known as spin (Prince and Links, 2015). Due to this spin, they also possess a microscopic magnetic field. This is represented by $\boldsymbol{\mu}$, which is a vector that describes the magnetic moment of a spinning nucleus.

$$\boldsymbol{\mu} = \gamma \boldsymbol{\phi} \tag{2.1}$$

where γ is a physical constant called the gyromagnetic ratio, which has a unique value for each nucleus. Moreover, this value is related to γ which is more widely used with units Hz per Tesla.

$$\gamma = \frac{\gamma}{2\pi} \tag{2.2}$$

Table. 2.1 shows the gyromagnetic ratios for some of the more prevalent atoms in the body. MRI only utilises signals from ^1H atoms in the body, which are abundant mostly in the form of water and other organic compounds. Moreover, it also has the largest gyromagnetic ratio which will result in the largest bulk magnetization **M** as shown next.

Table 2.1: Nuclei of atoms prevalent in the body which are useful for NMR (Zhi-Pei Liang)

Nucleus	Gyromagnetic ratio (MHz/T)
^1H	42.58
^{13}C	10.71
^{19}F	40.05
^{31}P	11.26

Normally, the magnetic moment of nuclei are all randomly oriented which causes the net magnetic field to be zero. Therefore, for $\boldsymbol{\mu}$ to be detectable, an external magnetic field $\mathbf{B}_0(\mathbf{r})$ is used to align all magnetic moments in one direction, in this case $\mathbf{i}_z$.

$$\mathbf{B}_0(\mathbf{r}) = B_0\mathbf{i}_z \tag{2.3}$$

Consequently, this produces a bulk magnetization $\mathbf{M}(\mathbf{r}, t)$ which is proportional to μ

$$\mathbf{M}(\mathbf{r}, t) = \sum_{n=1}^{N_s} \boldsymbol{\mu}_n \tag{2.4}$$

where N_s is the total number of spins.

The last part of NMR is resonance. At this point, the atoms are in equilibrium where $\mathbf{B}_0(\mathbf{r})$ and $\mathbf{M}(\mathbf{r}, t)$ are parallel to each other. After equilibriun is achieved, a second external magnetic field $\mathbf{B}_a(\mathbf{r}, t)$ called a radio-frequency field (RF field) is used. This RF field operates at a frequency $\omega_0(\mathbf{r})$ called the Larmor frequency.

$$\omega_0(\mathbf{r}) = \gamma B_0(\mathbf{r}) \tag{2.5}$$

The Larmor frequency is otherwise known as the natural frequency of a spin system and is the basis for nucleus specificity (Liang and Lauterbur, 2000). Following table. 2.1, suppose a body is placed in a background field of $B_0 = 1T$. In this case, ^1H and ^{31}P resonate at 42.58 MHz and 11.26 MHz respectively. This difference in resonance frequency allows signals from the two atoms to be distinguished from each other. Moreover, $\mathbf{B}_a(\mathbf{r}, t)$ causes $\mathbf{M}(\mathbf{r}, t)$ to be perpendicular to $\mathbf{B}_0(\mathbf{r})$.

When $\mathbf{B}_a(\mathbf{r}, t)$ is turned off, $\mathbf{M}(\mathbf{r}, t)$ starts to precess around $\mathbf{B}_0(\mathbf{r})$ until they are both parallel again. During this relaxation phase, the atoms emit a radio signal that is detectable by receiver coils in a phenomenon called free induction decay (FID). This signal is what allows MR images to be produced. Different materials take a different amount of time to return to equilibrium which consequently, creates contrast between different parts of the body.

2.2. BLOCH EQUATION

Initially, at $t = 0$, the system is in equilibrium with a static background field following Eq. 2.3. Moreover, the magnetization $\mathbf{M}$(r,t) of the system is currently:

$$\mathbf{M}(\mathbf{r}, t) = M_x^0\mathbf{i}_x + M_y^0\mathbf{i}_y + M_z^0\mathbf{i}_z \tag{2.6}$$

Subsequently, the system also receives an RF field $\mathbf{B}_a(\mathbf{r}, t)$. Therefore, the resulting magnetic field becomes:

$$\mathbf{B}(\mathbf{r}, t) = \mathbf{B}_0(\mathbf{r}) + \mathbf{B}_a(\mathbf{r}, t) \tag{2.7}$$

The Bloch equation is fundamental to describing the nuclear magnetization $\mathbf{M}(\mathbf{r}, t)$ as a function of time at each point in the system and forms the basis by which a signal is acquired from the body. The Bloch equation is:

$$\frac{\partial \mathbf{M}(\mathbf{r}, t)}{\partial t} + \gamma \mathbf{B}(\mathbf{r}, t) \times \mathbf{M}(\mathbf{r}, t) + \frac{1}{T_2(\mathbf{r})}\mathbf{M}_\perp(\mathbf{r}, t) + \frac{1}{T_1(\mathbf{r})}\mathbf{M}_\parallel(\mathbf{r}, t)\mathbf{i}_z = \frac{1}{T_1(\mathbf{r})}M^{eq}(\mathbf{r})\mathbf{i}_z \tag{2.8}$$

where T_1 and T_2 describe the longitudinal and transverse relaxation times respectively, and the magnetization is also separated into its transverse and longitudinal components.

$$\begin{aligned} \mathbf{M}_\perp(\mathbf{r}, t) &= M_x(\mathbf{r}, t)\mathbf{i}_x + M_y(\mathbf{r}, t)\mathbf{i}_y \\ \mathbf{M}_\parallel(\mathbf{r}, t) &= M_z(\mathbf{r}, t)\mathbf{i}_z \end{aligned} \tag{2.9}$$

In addition to this, the equilibrium magnetization M^{eq} is:

$$M^{eq}(\mathbf{r}) = \rho(\mathbf{r})\frac{\gamma^2\hbar^2}{4kT}B_0(\mathbf{r}) \tag{2.10}$$

where $\rho(\mathbf{r})$ is the density of spins per unit volume, $\hbar$ is Planck's constant divided by 2π, k is Boltzmann's constant, and T is the absolute temperature.

First, we solve the Bloch equation while ignoring relaxation effects. As a result, we can find the magnetization at each direction:

$$\begin{aligned} M_x(t) &= M_x^0 \cos(\omega_0(\mathbf{r})t) + M_y^0 \sin(\omega_0(\mathbf{r})t) \\ M_y(t) &= M_y^0 \cos(\omega_0(\mathbf{r})t) - M_x^0 \sin(\omega_0(\mathbf{r})t) \\ M_z(t) &= M_z^0 \end{aligned} \tag{2.11}$$

From this solution, we can conclude that the magnetization is precessing around the $\mathbf{i}_z$ direction, or $\mathbf{B}_0(\mathbf{r})$, in a left-handed manner with an angular frequency equal to the Larmor frequency $\omega_0(\mathbf{r})$.

2.3. ROTATING FRAME OF REFERENCE

Since the magnetization is constantly precessing around $\mathbf{B}_0(\mathbf{r})$, it is easier to use a rotating frame of reference instead of a static one to solve the Bloch equation While $\mathbf{i}_x$, $\mathbf{i}_y$, and $\mathbf{i}_z$ is used for the static frame, the apostrophe will be used to indicate the rotating frame. $\mathbf{i}'_x$, $\mathbf{i}'_y$, and $\mathbf{i}'_z$ are the directional vectors in the rotating frame.

$$\begin{bmatrix} \mathbf{i}_x \\ \mathbf{i}_y \\ \mathbf{i}_z \end{bmatrix} = \begin{bmatrix} cos(\omega_0(\mathbf{r})t) & sin(\omega_0(\mathbf{r})t) & 0 \\ -sin(\omega_0(\mathbf{r})t) & cos(\omega_0(\mathbf{r})t) & 0 \\ 0 & 0 & 1 \end{bmatrix} \begin{bmatrix} \mathbf{i}'_x \\ \mathbf{i}'_y \\ \mathbf{i}'_z \end{bmatrix} \tag{2.12}$$

Therefore, it can be seen that the rotating frame of reference is **R**:

$$R = \begin{bmatrix} cos(\omega_0(\mathbf{r})t) & sin(\omega_0(\mathbf{r})t) & 0 \\ -sin(\omega_0(\mathbf{r})t) & cos(\omega_0(\mathbf{r})t) & 0 \\ 0 & 0 & 1 \end{bmatrix} \tag{2.13}$$

Meanwhile, the magnetization can be shown in a matrix

$$m = [M_x, M_y, M_z]^T \quad \text{and} \quad m' = [M'_x, M'_y, M'_z]^T$$

where

$$m = Rm' \quad \text{and} \quad m' = R^T m$$

Moreover, it is important to note that $R^{-1} = R^T$.
Now we come back to the Bloch equation Firstly, the Bloch equation is separated into its vector counterparts:

$$\frac{\partial M_x}{\partial t} - \omega_0(\mathbf{r})M_y + \frac{1}{T_2}M_x = 0 \tag{2.14}$$

$$\frac{\partial M_y}{\partial t} + \omega_0(\mathbf{r})M_x + \frac{1}{T_2}M_y = 0 \tag{2.15}$$

$$\frac{\partial M_z}{\partial t} + \frac{1}{T_1}M_z = \frac{1}{T_1}M^{eq} \tag{2.16}$$

This can also be seen in matrix form as:

$$\frac{\partial m}{\partial t} + \omega_0(\mathbf{r}) \begin{bmatrix} 0 & -1 & 0 \\ 1 & 0 & 0 \\ 0 & 0 & 0 \end{bmatrix} m + \begin{bmatrix} \frac{1}{T_2} & 0 & 0 \\ 0 & \frac{1}{T_2} & 0 \\ 0 & 0 & \frac{1}{T_1} \end{bmatrix} m = \begin{bmatrix} 0 \\ 0 \\ \frac{1}{T_1}M^{eq} \end{bmatrix} \tag{2.17}$$

Substituting $m = Rm'$ results in:

$$(R\frac{\partial m'}{\partial t} + \frac{\partial R}{\partial t}m') + \omega_0(\mathbf{r}) \begin{bmatrix} 0 & -1 & 0 \\ 1 & 0 & 0 \\ 0 & 0 & 0 \end{bmatrix} Rm' + \begin{bmatrix} \frac{1}{T_2} & 0 & 0 \\ 0 & \frac{1}{T_2} & 0 \\ 0 & 0 & \frac{1}{T_1} \end{bmatrix} Rm' = \begin{bmatrix} 0 \\ 0 \\ \frac{1}{T_1}M^{eq} \end{bmatrix} \tag{2.18}$$

To simplify this equation, we notice the following relation:

$$\frac{\partial R}{\partial t} + \omega_0(\mathbf{r}) \begin{bmatrix} 0 & -1 & 0 \\ 1 & 0 & 0 \\ 0 & 0 & 0 \end{bmatrix} R = 0 \tag{2.19}$$

As a result, Eq. 2.18 becomes:

$$R\frac{\partial m'}{\partial t} + \begin{bmatrix} \frac{1}{T_2} & 0 & 0 \\ 0 & \frac{1}{T_2} & 0 \\ 0 & 0 & \frac{1}{T_1} \end{bmatrix} Rm' = \begin{bmatrix} 0 \\ 0 \\ \frac{1}{T_1}M^{eq} \end{bmatrix} \tag{2.20}$$

And subsequently, multiplying by R^T results in:

$$\frac{\partial m'}{\partial t} + \begin{bmatrix} \frac{1}{T_2} & 0 & 0 \\ 0 & \frac{1}{T_2} & 0 \\ 0 & 0 & \frac{1}{T_1} \end{bmatrix} m' = \begin{bmatrix} 0 \\ 0 \\ \frac{1}{T_1} M^{eq} \end{bmatrix} \tag{2.21}$$

Taken out of the matrix and separated into its vector counterparts results in:

$$\frac{\partial M'_x}{\partial t} + \frac{1}{T_2} M'_x = 0 \tag{2.22}$$

$$\frac{\partial M'_y}{\partial t} + \frac{1}{T_2} M'_y = 0 \tag{2.23}$$

$$\frac{\partial M'_z}{\partial t} + \frac{1}{T_1} M'_z = \frac{1}{T_1} M^{eq} \tag{2.24}$$

Then we solve the first-order partial differential equation for each of the directions to get:

$$M'_x = M^0_x e^{(-t/T_2)} \tag{2.25}$$

$$M'_y = M^0_y e^{(-t/T_2)} \tag{2.26}$$

$$M'_z = M^0_z e^{(-t/T_1)} + (1 - e^{(-t/T_1)}) M^{eq} \tag{2.27}$$

And finally, by using Eq. 2.11 and the relation that $m' = R^T m$, the magnetization is:

$$\begin{aligned} M_x(t) &= e^{(-t/T_2)} [M^0_x cos(\omega_0(\mathbf{r})\, t) + M^0_y sin(\omega_0(\mathbf{r})\, t)] \\ M_y(t) &= e^{(-t/T_2)} [M^0_y cos(\omega_0(\mathbf{r})\, t) - M^0_x sin(\omega_0(\mathbf{r})\, t)] \\ M_z(t) &= M^0_z e^{(-t/T_1)} + (1 - e^{(-t/T_1)}) M^{eq} \end{aligned} \tag{2.28}$$

2.4. FREE INDUCTION DECAY

Having solved the magnetization from the Bloch equation in the last section, we can now find the resulting voltage $V(t)$ in a receiver coil. This signal is called the free induction decay signal, as described in the section explaining NMR.

$$\begin{aligned} V(t) &= -\int \frac{\partial \mathbf{M}(\mathbf{r}, t)}{\partial t} \cdot B_r(\mathbf{r})\, d\mathbf{r} \\ V(t) &= -\int (\frac{\partial M_x}{\partial t} B_{r,x} + \frac{\partial M_y}{\partial t} B_{r,y} + \frac{\partial M_z}{\partial t} B_{r,z})\, d\mathbf{r} \end{aligned} \tag{2.29}$$

where $B_r(\mathbf{r})$ is the so-called receiver coil sensitivity.
Following Eq. 2.28, the derivative of M_x is:

$$\begin{aligned} \frac{\partial M_x}{\partial t} &= \omega_0(\mathbf{r}) e^{(-t/T_2)} [-M^0_x sin(\omega_0(\mathbf{r})\, t) + M^0_y cos(\omega_0(\mathbf{r})\, t)] \\ &\quad - \frac{1}{T_2} e^{(-t/T_2)} [M^0_x cos(\omega_0(\mathbf{r})\, t) + M^0_y sin(\omega_0(\mathbf{r})\, t)] \end{aligned} \tag{2.30}$$

Typically, $\omega_0(\mathbf{r}) \gg \frac{1}{T_2}$ which results in:

$$\frac{\partial M_x}{\partial t} \approx \omega_0(\mathbf{r}) e^{(-t/T_2)} [-M_x^0 sin(\omega_0(\mathbf{r})\, t) + M_y^0 cos(\omega_0(\mathbf{r})\, t)] \tag{2.31}$$

and similarly, the derivative of M_y becomes:

$$\frac{\partial M_y}{\partial t} \approx -\omega_0(\mathbf{r}) e^{(-t/T_2)} [M_y^0 sin(\omega_0(\mathbf{r})\, t) + M_x^0 cos(\omega_0(\mathbf{r})\, t)] \tag{2.32}$$

Moreover, usually $\omega_0(\mathbf{r}) \gg \frac{1}{T_1}$,and therefore the derivative of M_z can be seen as negligible. This results in:

$$\begin{aligned} V(t) \approx -\int -\omega_0(\mathbf{r}) e^{(-t/T_2)} \{ &[M_x^0 sin(\omega_0(\mathbf{r}))\, t) - M_y^0 cos(\omega_0(\mathbf{r}))\, t)] B_{r,x} \\ &+ [M_x^0 cos(\omega_0(\mathbf{r}))\, t) + M_y^0 sin(\omega_0(\mathbf{r}))\, t)] B_{r,y} \}\, d\mathbf{r} \end{aligned} \tag{2.33}$$

Introducing the complex field quantities

$$M_0^{\pm} = M_x^0 \pm j M_y^0 \quad \text{and} \quad B_{r,xy}^{\pm} = B_x \pm j B_y$$

$V(t)$ can be written as:

$$V(t) \approx \frac{j}{2} \int \omega_0(\mathbf{r}) e^{(-t/T_2)} (e^{-j\omega_0(\mathbf{r}))\, t} M_0^+ B_{r,xy}^- - e^{j\omega_0(\mathbf{r}))\, t} M_0^- B_{r,xy}^+)\, d\mathbf{r} \tag{2.34}$$

The signal is then amplified, and demodulated with a demodulation frequency ω_{mod}.

$$V_{demod}(t) = 2A e^{\omega_{mod}\, j\, t} V(t) \tag{2.35}$$

Subsequently, the signal is passed through a low-pass filter resulting in the following signal model:

$$S(t) = jA \int \omega_0(\mathbf{r}) e^{(-t/T_2)} e^{-\triangle\omega_0(\mathbf{r})\, j\, t} M_0^+ B_{r,xy}^-\, d\mathbf{r} \tag{2.36}$$

where $\triangle\omega_0(\mathbf{r}) = \omega_0(\mathbf{r}) - \omega_{mod}$. Here, the scaling constant $jA\omega_0(\mathbf{r})$ can be omitted. Moreover, the receiver coils are assumed to have uniform sensitivity, and the transverse relaxation effects can be ignored for simplicity (Liang and Lauterbur, 2000). Doing this omits $B_{r,xy}^-$ and $e^{(-t/T_2)}$ respectively, resulting in the following signal expression:

$$S(t) = \int e^{-\triangle\omega_0(\mathbf{r})\, j\, t} M_0^+\, d\mathbf{r} \tag{2.37}$$

A spin density map $\rho(\mathbf{r})$ can be used to describe the transverse magnetization M_0^+, which results in the received signal model:

$$S(t) = \int \rho(\mathbf{r}) e^{-\triangle\omega_0(\mathbf{r})\, j\, t}\, d\mathbf{r} \tag{2.38}$$

Lastly, a change in the main magnetic field B_0 can cause a spatial variation in the Larmor frequency, and this can be expressed using an off-resonance map $\triangle B_0(\mathbf{r})$ (measured in

Hz, so γ can be omitted), which describes a change in the B_0 field from the resonance frequency.

$$\triangle B_0(\mathbf{r}) = B_0(\mathbf{r}) - B_{0,center} \tag{2.39}$$

Therefore, the resulting signal model becomes

$$S(t) = \int \rho(\mathbf{r}) e^{-2\pi \triangle B_0(\mathbf{r}) j t} \, d\mathbf{r} \tag{2.40}$$

2.5. SPATIAL ENCODING

Although a signal has been obtained, the location where the signal originated is still not known. To spatially encode the signal, gradient coils are used to produce a linearly varying field $G(\mathbf{r})$ along each direction (measured in Hz):

$$G(\mathbf{r}) = G_x \mathbf{i}_x + G_y \mathbf{i}_y + G_z \mathbf{i}_z \tag{2.41}$$

This results in the following vectorized spatially encoded signal

$$S(t,\tau,\upsilon) = \int \rho(\mathbf{r}) e^{-2\pi \triangle B_0(\mathbf{r}) j t} e^{-2\pi G_x(\mathbf{r}) j t} e^{-2\pi G_y(\mathbf{r}) j \tau} e^{-2\pi G_z(\mathbf{r}) j \upsilon} \, d\mathbf{r} \tag{2.42}$$

where t is the duration of each frequency encoding step, while τ and υ are the duration of each phase encoding step along the y- and z-axes.

2.6. APPROXIMATE INVERSE SIGNAL MODEL

At the end of spatial encoding, the signal in k-space notation can be seen as:

$$S(t,\tau,\upsilon) = \int \rho(\mathbf{r}) e^{-2\pi j (\triangle B_0(\mathbf{r}) t + \mathbf{k}(t)\mathbf{r})} \, d\mathbf{r} \tag{2.43}$$

where $\mathbf{k}(t)$ is the sum of its directional components:

$$\begin{aligned} k_x &= G_x t \\ k_y &= G_y \tau \\ k_z &= G_z \upsilon \end{aligned} \tag{2.44}$$

Eq. 2.43 shows that signal $S(t,\tau,\upsilon)$ is the Fourier transform of the spin density map along the trajectory $\mathbf{k}(t)$ with a phase shift $\triangle B_0(\mathbf{r})$ (Börnert et al., 1999). Therefore our inverse signal model can be approximated as:

$$\rho(\mathbf{r}) \approx \int\int\int S(t,\tau,\upsilon) e^{2\pi \triangle B_0(\mathbf{r}) j t} e^{2\pi G_x(\mathbf{r}) j t} e^{2\pi G_y(\mathbf{r}) j \tau} e^{2\pi G_z(\mathbf{r}) j \upsilon} \, dt \, d\tau \, d\upsilon \tag{2.45}$$

The signal model and the approximate inverse signal model that have been derived will be used in the next chapter for reconstruction.

3

RECONSTRUCTION

Now that the signal model is derived, the image can be reconstructed. Normally, a fast Fourier transform (FFT) based reconstruction is sufficient to transform the signal into the spatial domain and obtain an image. Unfortunately, this is not the case when inhomogeneities in the magnetic fields are present, as this would lead to a distorted image. Therefore, other image reconstruction techniques need to be used.

There are several image distortion correction techniques available, such as the model-based reconstruction (de Leeuw den Bouter et al., 2019) and conjugate phase reconstruction (CPR) (Maeda et al., 1988). While model-based reconstruction have been shown to be more effective for stronger inhomogeneities, CPR is able to correct an image faster because it incorporates FFT in its implementation (Koolstra et al., 2021). Therefore, for moderate inhomogeneities where CPR provides a sufficiently accurate reconstruction, CPR is more practical to use.

This section will first focus on how the B_0 and gradient field maps are processed, followed by how a distorted phantom is created for the simulation. And lastly, CPR will be explained.

3.1. ESTIMATED $\triangle B_0$ FIELD MAP

The low-field scanner that is being developed by O'Reilly et al. (2021) currently suffers from magnetic field inhomogeneity, particularly B_0 field inhomogeneity and gradient field non-linearity. Therefore, this needs to be taken into account in the signal model.

CPR requires the $\triangle B_0(\mathbf{r})$ field map prior to reconstruction, therefore a method to estimate the resulting field map is needed. One way to do this is by obtaining two images of the same object with a time-shift (Noll, 1991). This results in two phase maps, $\phi_1(\mathbf{r})$ at echo time TE_1 and $\phi_2(\mathbf{r})$ at echo time TE_2. Then the $\triangle B_0(\mathbf{r})$ field map is

$$\triangle B_0(\mathbf{r}) = \frac{\phi_2(\mathbf{r}) - \phi_1(\mathbf{r})}{TE_2 - TE_1} \tag{3.1}$$

A mask of the object is then made and fitted on top of the estimated field map, and in this way noise in the background is ignored. The low-field scanner has a lower magnetic field

strength than conventional MRI scanners, and this cause images from the scanner to have low SNR. While this method can quickly obtain the $\triangle B_0(\mathbf{r})$ field map, it can lead to an inaccurate field map when the image has noise. To reduce noise, a sine-bell squared filter is used which removes high-frequency components from the k-space data.

3.1.1. SPHERICAL HARMONICS

The estimated field map is in the shape of the image (or in the case of the simulations, the $\triangle B_0(\mathbf{r})$ field map is in the shape of the bore). Reconstruction by FFT and CPR require the field map to cover the whole FOV, therefore, a method is needed to expand the field map. One way to do this is by fitting the obtained or estimated field map through a basis of second-order spherical harmonics. The theory behind spherical harmonics is not covered in this thesis. MATLAB code developed in LUMC by Tom O'Reilly was used as a basis for the spherical harmonics used in this paper. More information on spherical harmonics can be found in (Koolstra et al., 2021).

3.2. CONJUGATE PHASE RECONSTRUCTION

Conjugate phase reconstruction (CPR) is a method for correcting the accumulation of phase errors caused by magnetic field inhomogeneity. To do this, the phase error parts of the field maps need to be separated. For the B_0 field map, this can be done according to Equation 2.39.

Let us first take a look at CPR for B_0 inhomogeneity, where the effective phase error $w_{eff}(\mathbf{r}) = \triangle B_0(\mathbf{r})$, and $\triangle B_0(\mathbf{r})$ is the estimated, or given, field map with a known matrix dimension of $m \times n \times l$. Then, the inverse signal model can be seen as

$$\rho(\mathbf{r}) \approx \int S(t) e^{2\pi w_{eff}(\mathbf{r}) j t} \, dt \tag{3.2}$$

Now, let $w(i)$ be w_{eff} flattened out along one axis and sorted by order of magnitude, where i represents an index with a range of 1 to $m \times n \times l$.

$$w(i) = w_{eff,min} \rightarrow w_{eff,max} \tag{3.3}$$

By using $w(i)$, a set of images $I_i(\mathbf{r})$ can be reconstructed

$$I_i(\mathbf{r}) \approx \int S(t) e^{2\pi w(i) j t} \, dt \tag{3.4}$$

Now, we have created $m \times n \times l$ images, one for each off-resonance frequency and the CPR corrected image can be reconstructed pixel by pixel. This is done by taking a pixel $I_i(\mathbf{r}_i)$ from each off-resonance image, where position $\mathbf{r}_i$ corresponds to the same position where $w(i) = w_{eff}(\mathbf{r}_i)$. As a result, each pixel of the CPR corrected image has a magnitude which is consistent with the off-resonance frequency at that location. This is further illustrated in Figure 3.1. Nevertheless, creating $m \times n \times l$ images is a costly operation that can take a long time. To speed up the process, frequency segmented reconstruction (FSR) (Noll, 1991) and multifrequency interpolation (MFI) (Man et al., 1997) is explored.

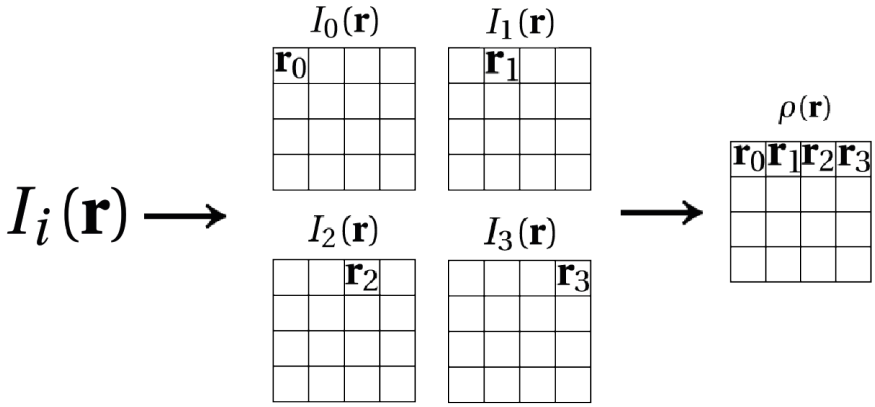

Figure 3.1: The inverse Fourier transform of the signal S(t) along the trajectory $w(i)$ creates a set of images $I_i(\mathbf{r})$, where each pixel $\mathbf{r}_i$ from image $I_i(\mathbf{r})$ becomes a pixel in $\rho(\mathbf{r})$ at position $\mathbf{r}_i$

3.2.1. FREQUENCY SEGMENTED RECONSTRUCTION

Looking back at Equation 3.2, it can be seen that an image $\rho(\mathbf{r})$ is the result of a signal $S(t)$ multiplied by a phase of $2\pi w_{eff} t$, where w_{eff} represents the off-resonance frequencies, and t is the readout time with a range of $0 \rightarrow T$. Therefore, the maximum phase error that can be achieved is at $2\pi w_{eff,max} T$. In FSR, the range of off-resonance frequencies $w(i)$ is discretized into $L+1$ equally spaced segments, such that the accumulation of phase error in each segment is sufficiently small so that the resulting images $I_i(\mathbf{r})$ will still be a good approximation

$$2\frac{2\pi w_{eff,max} T}{L} < \frac{\pi}{2} \tag{3.5}$$

A factor two is added since off-resonance frequencies range from negative to positive frequencies. As a result, $w(i)$ is divided into $L_{FSR}+1$ segments

$$L_{FSR} > 4\frac{(2\pi \triangle w_{max}) T}{\pi} \tag{3.6}$$

In other words, $w(i)$ is still the same as Equation 3.3 but now i represents an index with a range of 1 to $L_{FSR}+1$.

3.2.2. MULTIFREQUENCY INTERPOLATION

MFI is a similar CPR technique to FSR. It aims to reduce computation time by reducing the number of images $I_i(\mathbf{r})$ that have to be produced. To make up for this, coefficients $c_i(\triangle w)$ have to be computed. In the end, the CPR corrected image I_{cp} is computed as

$$I_{cp}(\mathbf{r}) \approx \sum_{i=0}^{L_{MFI}} c_i(\triangle w(\mathbf{r})) I_i(\mathbf{r}) \tag{3.7}$$

The coefficients $c_i(\triangle w)$ can be chosen such that the following equation holds approximately

$$e^{2\pi \triangle w j t} \approx \sum_{i=0}^{L_{MFI}} c_i(\triangle w) e^{2\pi w(i) j t} \tag{3.8}$$

where $\triangle w$ is the full range of off-resonance frequencies and $w(i)$ is the range of off-resonance frequencies discretized into less segments than in FSR. While FSR gives a threshold of $\frac{\pi}{2}$ for the accumulation of phase error in a segment, MFI takes advantage of the periodic nature of the signal and sets the threshold to 2π instead.

$$2\frac{2\pi w_{eff,max}T}{L} < 2\pi \tag{3.9}$$

Therefore, the off-resonance frequencies are divided into $L_{MFI}+1$ segments, a decrease by a factor of 4 compared to FSR.

$$L_{MFI} > \frac{(2\pi\triangle w_{max})T}{\pi} \tag{3.10}$$

The coefficients $c_i(\triangle w)$ can be approximated by least squares, for which many algorithms exist. To do this, Equation 3.8 can be seen to fit the least squares equation $Ax = b$, where

$$\begin{aligned} A &= e^{2\pi w(i)jt} \\ x &= c_i(\triangle w) \\ b &= e^{2\pi\triangle wjt} \end{aligned} \tag{3.11}$$

3.2.3. ADDITIONAL GRADIENT NON-LINEARITY CORRECTION

The above methods can also be extended to correct for gradient non-linearity. The gradient field maps consist of a linear and non-linear part. Therefore, the non-linear part can be obtained by taking the difference between the gradient field map and it's perfectly linear version.

$$G_{r,nonlinear} = G_r - G_{r,linear} \tag{3.12}$$

Consequently, this results in the inverse signal model below

$$\begin{aligned} \rho(\mathbf{r}) \approx \int\int\int S(t) e^{2\pi(\triangle B_0(\mathbf{r})+G_{x,nonlinear}(\mathbf{r}))jt} e^{2\pi G_{x,linear}(\mathbf{r})jt} \\ e^{2\pi G_{y,nonlinear}(\mathbf{r})j\tau} e^{2\pi G_{y,linear}(\mathbf{r})j\tau} \\ e^{2\pi G_{z,nonlinear}(\mathbf{r})j\upsilon} e^{2\pi G_{z,linear}(\mathbf{r})j\upsilon}\, dt\, d\tau\, d\upsilon \end{aligned} \tag{3.13}$$

The reconstruction can be divided into three parts concerning each of the gradient field directions. As a result, the effective phase error w_{eff} for each direction is

$$\begin{aligned} w_{eff,1}(\mathbf{r}) &= \triangle B_0(\mathbf{r}) + G_{x,nonlinear}(\mathbf{r}) \\ w_{eff,2}(\mathbf{r}) &= G_{y,nonlinear}(\mathbf{r}) \\ w_{eff,3}(\mathbf{r}) &= G_{z,nonlinear}(\mathbf{r}) \end{aligned} \tag{3.14}$$

Each w_{eff} is corrected for one by one. Similarly, w_{eff} is flattened out and sorted by order of magnitude into $w(i)$. And, depending on the method, the index i will range from 1 to $m \times n \times l$ for full CPR, or $1 \rightarrow L_{FSR}+1$ or $1 \rightarrow L_{MFI}+1$.

4

SIMULATION

To test the application of the reconstruction algorithms, two simulations are done. The first simulation covers B_0 field inhomogeneity, and the second simulation covers both B_0 field inhomogeneity and gradient field non-linearity.

4.1. DISTORTED PHANTOM

The Shepp-Logan phantom is a standard test image that is modelled to provide similar contrast to in vivo images of a human head, therefore it is a good starting point to test the effectiveness of an image reconstruction algorithm. The currently used phantom (Schabel, 2006) has a dimension of $128 \times 128 \times 30$ voxels (this dimension is also used subsequently in the creation of the $\triangle B_0$ and non-linear gradient field maps).

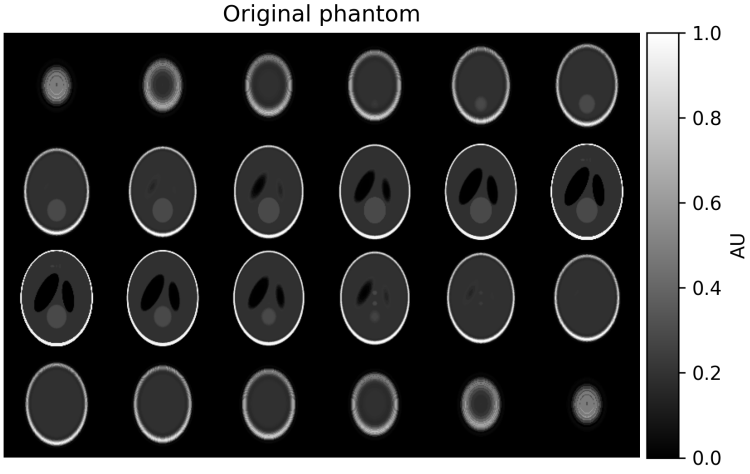

Figure 4.1: Original Shepp-Logan phantom used in simulations (Schabel, 2006).

4.1.1. $\triangle B_0$ FIELD MAP

The main magnetic field of the low-field scanner was measured with a resolution of $5 \times 5 \times 5$ mm^3 and field of view (FOV) of 225 x 225 x 300 mm^3 which is then truncated to an FOV of $200 \times 200 \times 200$ mm^3 to match the FOV of the gradient field maps. It was obtained by using a gaussmeter (Lake Shore Cryotronics, Westerville, OH) connected to a 3D positioning robot, and is subsequently converted to Hz (Koolstra et al., 2021). Then, the centre frequency was subtracted from the field map to create the $\triangle B_0$ field map shown in Figure 4.2a. A field map spanning the whole FOV is required for reconstruction. Therefore, the $\triangle B_0$ field map is fitted to a basis of second-order spherical harmonics resulting in the $\triangle B_0$ field map used for the simulation shown in Figure 4.2b.

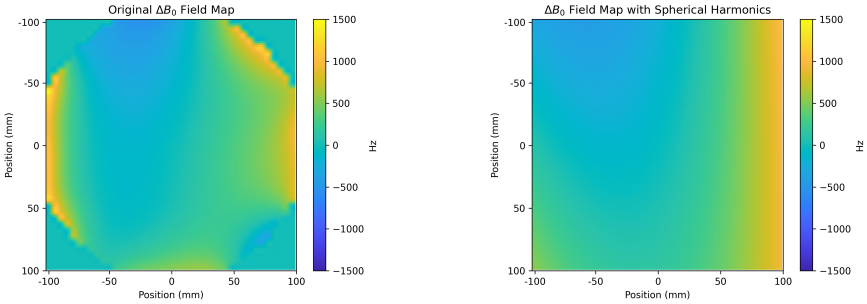

(a) Original $\triangle B_0$ field map

(b) $\triangle B_0$ field map fitted to spherical harmonics

Figure 4.2: **a** The measured $\triangle B_0$ field map of the low-field scanner **b** The $\triangle B_0$ field map expanded to span the whole FOV by fitting the $\triangle B_0$ field map to a basis of second-order spherical harmonics

4.1.2. GRADIENT FIELD MAPS

Shown in Figure 4.3 and 4.4, are non-linear gradient fields obtained by using the magnetostatic solver in CST Studio Suite (Darmstadt, Germany) to simulate the resulting field maps from the gradient coils. The field map has a resolution of $5 \times 5 \times 5$ mm^3 and an FOV of $200 \times 200 \times 200$ mm^3. The reconstruction algorithm requires the non-linear part of the gradients to be separated from the obtained gradient field maps. To do this, a perfectly linear gradient field map with the same FOV and resolution is simulated. This is then subtracted from the obtained gradient field maps which results in the separated gradient non-linearity.

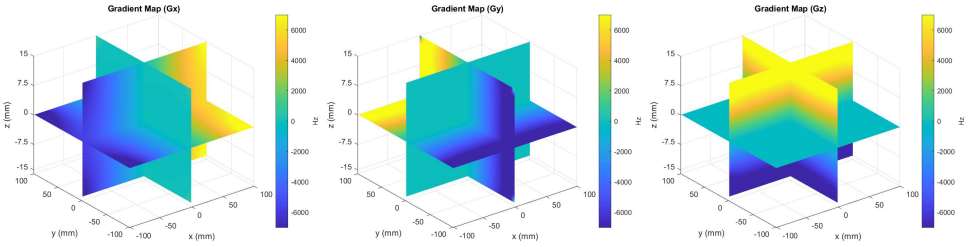

Figure 4.3: Simulated gradient field maps from CST Studio Suite (Darmstadt, Germany).

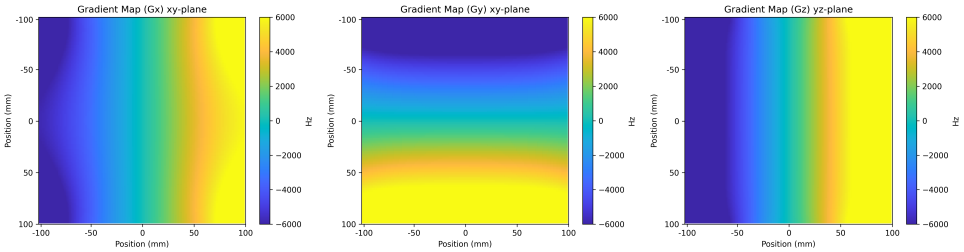

Figure 4.4: Middle slice of simulated gradient field maps.

4.1.3. DISTORTED PHANTOM

With the $\triangle B_0$ and non-linear gradient field maps, a distorted phantom can be simulated. Two distorted phantoms are made. The first one exhibits distortions only due to B_0 inhomogeneity, shown in Figure 4.5a, and the second one exhibits distortions due to both B_0 inhomogeneity and gradient field non-linearity, shown in Figure 4.5b.

4.2. CONJUGATE PHASE RECONSTRUCTION

As previously described, CPR discretizes the range of off-resonance frequencies into $L+1$ equally-spaced segments. Then, $L+1$ images are reconstructed using inverse FFT. A voxel is taken from each resulting image which corresponds to a voxel of approximately the same reconstruction frequency in the field map. This is done until all voxels are acquired which results in the CPR corrected image.

This section shows the results of three CPR methods, each one with less frequency segments. The first method is full CPR, which takes the frequency of each voxel in the field map and uses it to create an image. This results in a very long reconstruction time, but nevertheless, shows the limits of the CPR technique. The second method is FSR where the range of off-resonance frequencies is divided into $L_{FSR}+1$ segments.

$$L_{FSR} > 4\frac{(2\pi\triangle w_{max})T}{\pi} \tag{4.1}$$

And the third method is MFI, which divides the range of off-resonance frequencies into $L_{MFI}+1$ segments and requires coefficients $c_i(\triangle w)$ to be computed to make up for the reduced number of frequency segments.

$$L_{MFI} > \frac{(2\pi\triangle w_{max})T}{\pi} \tag{4.2}$$

The resulting corrected images of each method give visually similar images. To compare them better, the following image is made

$$\frac{||Full\,CPR| - |Corrected\,image||}{|Full\,CPR|} \tag{4.3}$$

and the resulting images are shown in Figure 4.6 for the B_0 field distorted phantom, and in Figure 4.7 for the B_0 and gradient field distorted phantom.

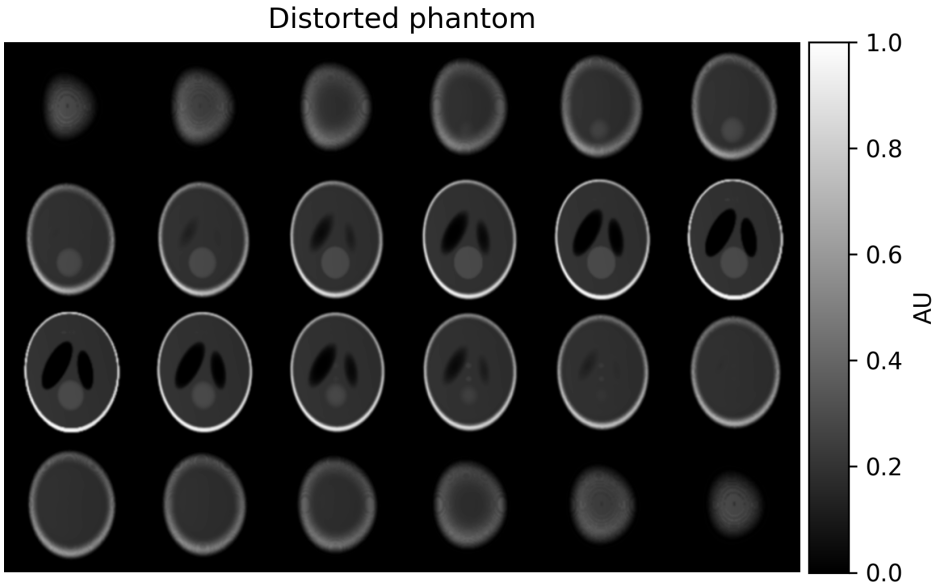

(a) Distorted phantom from $\triangle B_0$ inhomogeneity.

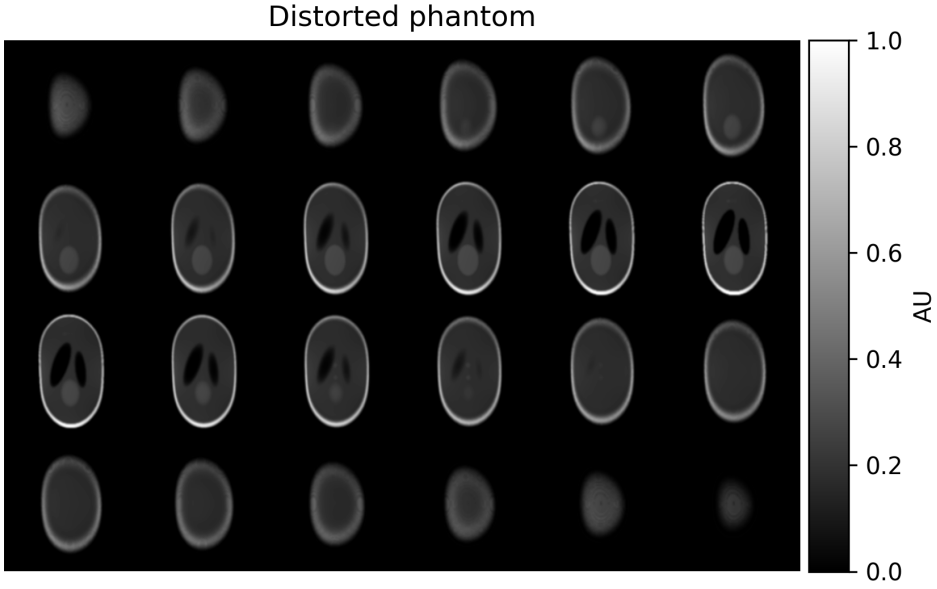

(b) Distorted phantom from both $\triangle B_0$ inhomogeneity and gradient field non-linearity.

Figure 4.5: Simulated distorted phantoms.

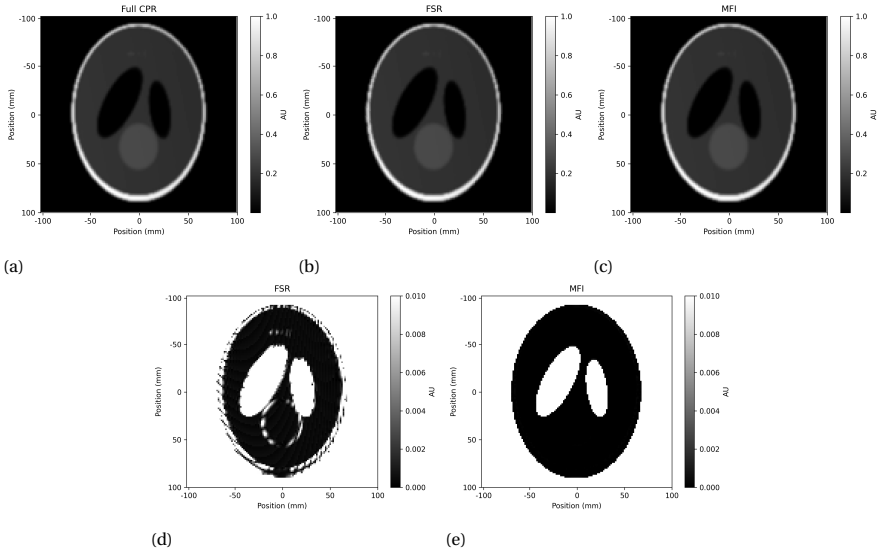

Figure 4.6: $\triangle B_0$ field corrected phantom. **a**, **b**, **c** shows visually similar results for the three CPR methods. **c** and **d** show the FSR and MFI method compared to full CPR method respectively using Equation 4.3

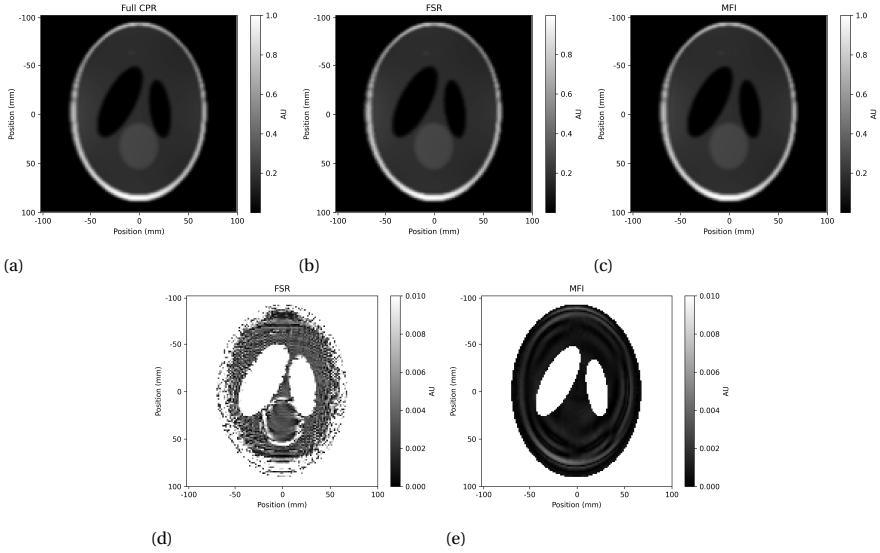

Figure 4.7: $\triangle B_0$ and non-linear gradient field corrected phantom. **a**, **b**, **c** shows visually similar results for the three CPR methods. **c** and **d** show the FSR and MFI method compared to full CPR method respectively using Equation 4.3

Looking at Figures. 4.6d and 4.6e one can see that the MFI method produces a more accurate image than the FSR method. The FSR method shows more blurring in the out-

lines of the phantom. This can be seen more prominently in Figures. 4.7d and 4.7e where on top of blurring of the outline, there is also a lot of noise seen inside the phantom. On the other hand, the MFI method exhibit ringing artifacts which can be interpreted as the effect of taking fewer frequency segments than FSR, as well as the added gradient non-linearity, but fortunately this is not visible in the final image.

4.3. PERFORMANCE

The basis by which the best method is chosen relies on the image quality, as ideally the reconstruction algorithm should correct all distortion. Nevertheless, another important criteria is speed, because a reconstruction method is not viable if it takes too long. Based on these two criteria, the best CPR method is chosen to be used for in vivo images.

4.3.1. RESIDUAL ERROR

A quantitative approach can also be used to differentiate between the methods. Although it is not possible to obtain the original not distorted image for in vivo, one advantage of doing simulations is that the original not distorted image is available. Therefore, this can be used to compare the resulting corrected images. One method to calculate the residual error is by using an alternate form of the Frobenius norm which takes into account the third dimension. This is given by

$$||A||_F = \sqrt{\sum_{i=0}^{m}\sum_{j=0}^{n}\sum_{k=0}^{l}|a_{i,j,k}|^2} \tag{4.4}$$

where A is the norm of a data set with dimensions $m \times n \times l$. The resulting residual norm error can then be described as

$$\epsilon = \frac{||original - corrected||_F}{||original||_F} \tag{4.5}$$

Table. 4.1 shows the resulting residual norm error of each reconstruction method while excluding the background.

Method	Residual norm error
Distorted phantom	0.566
Full CPR	0.389
FSR	0.389
MFI	0.389

(a) $\triangle B_0$

Method	Residual norm error
Distorted phantom	0.874
Full CPR	0.430
FSR	0.432
MFI	0.430

(b) $\triangle B_0$ + gradient

Table 4.1: Residual norm error of each reconstruction method

Looking at Table. 4.1a, the residual norm error of each reconstruction method stays consistent, meaning that both FSR and MFI provide reconstruction as good as full CPR. On the other hand, Table. 4.1b shows an increase of 0.002 for FSR when non-linear gradient fields are involved, while MFI still stays consistent with full CPR. This shows the efficacy of the coefficients used in MFI.

4.3.2. SPEED

The reconstruction was done with a computer that has an Intel Core i7-4710MQ @2.5 GHz and 16 GB of internal memory, and the speed of each reconstruction method is shown below

Method	Duration
Full CPR	9h 49m 29.8s
FSR	34.9s
MFI	2m 56.2s

(a) $\triangle B_0$

Method	Duration
Full CPR	18h 54m 10.8s
FSR	1m 9.3s
MFI	3m 6.7s

(b) $\triangle B_0$ + gradient

Table 4.2: Duration of each reconstruction method

Full CPR does not divide the available range of off-resonance frequencies and therefore needs to produce the most number of images, which results in the full CPR method requiring the longest amount of time to run. As opposed to full CPR, FSR requires significantly less images. This is reflected in the amount of time it takes to complete FSR. Meanwhile, although MFI requires the least amount of images between the three methods, it also requires the calculation of compensating coefficients through least-squares which results in a slower implementation. Originally, the least-squares function from Numpy was used $numpy.linalg.lstsq$ and this resulted in computation times of 2h 37m for correcting the $\triangle B_0$ and gradient field distorted phantom. The conjugate gradient least squares function from Scipy, $scipy.sparse.linalg.cgs$, significantly reduces the computation time to 9m 30s while maintaining the same image and residual error. Further optimisation can be done by looking at Equation 3.8. While $\triangle w$ calls for the full range of off-resonance frequencies, rounding the frequencies to 1 decimal place results in more overlap in frequencies of different pixels, for example, instead of creating 2 images for 2 pixels of the field map, 1 image can be made when the frequency of the 2 pixels are the same. Doing this reduces the duration of MFI to 3m 6.7s while having a negligible increase in the resulting residual norm error.

Table. 4.3 shows the duration of each step for FSR and MFI. Looking at the duration of correcting for $w_{eff,2}$ and $w_{eff,3}$ shows how the speed of reconstruction depends on the magnitude of inhomogeneity. Nevertheless, despite $w_{eff,1}$ having a smaller magnitude of off-resonance than $w_{eff,2}$, $w_{eff,1}$ takes longer due to accounting for $\triangle B_0$ as well, which shows that the speed of reconstruction also depends on the severity of inhomogeneity.

	w_{eff}	$\lvert w_{eff,max} \rvert$	FSR	MFI
$w_{eff,1}$	$\triangle B_0 + G_{x,nonlinear}$	12,724 Hz	49.1s	1m 59.4s
$w_{eff,2}$	$G_{y,nonlinear}$	15,189 Hz	15.6s	56.6s
$w_{eff,3}$	$G_{z,nonlinear}$	2,608 Hz	4.6s	10.7s

Table 4.3: Duration of each step for $\triangle B_0$ + gradient distorted phantom

4.3.3. FREQUENCY SEGMENTS VS RESIDUAL ERROR

While comparing the three reconstruction methods, one can also see the effect of reducing the number of frequency segments on the resulting residual norm error of the corrected image as shown in Figure 4.8. The plot shows that as the number of frequency segments increase, the residual norm error decreases until it starts to plateau, staying stable at $\epsilon = 0.389$. Moreover, CPR with L_{FSR} has the same residual norm error as full CPR despite using significantly less frequency segments. On the other hand, CPR with L_{MFI} is at a position where the residual norm error is starting to increase, which makes the calculation of the coefficients $c_i(\triangle w)$ necessary to maintain the same residual norm error as the plateau. Moreover, Figure 4.8 also shows the residual norm error of MFI as the green dotted line. It can be seen that MFI plateaus earlier than CPR, and also how the calculated L_{MFI} is able to predict when the plateau has occurred. Using the MFI coefficients effectively reduces the residual norm error at L_{MFI} from $\epsilon = 0.394$, to $\epsilon = 0.389$ which is the same as full CPR.

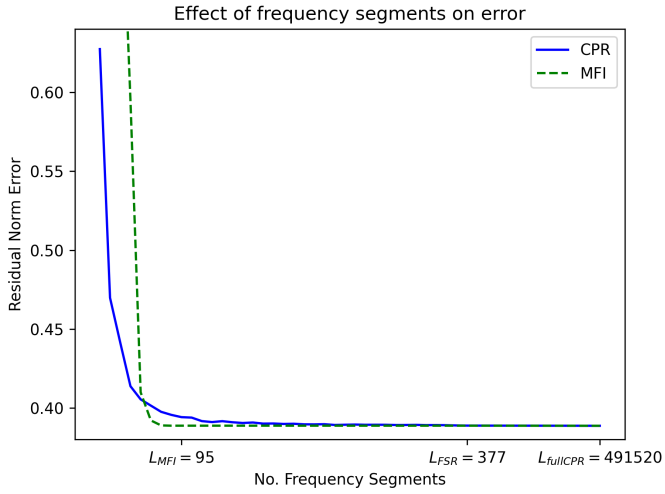

Figure 4.8: The effect of the number of frequency segments L on the residual norm error of the corrected image. CPR was done on a $\triangle B_0$ field distorted phantom.

5

Low-field MRI Data

While MFI returned better images in Figures. 4.6e and 4.7e, the resulting residual norm error of FSR and MFI is the same for $\triangle B_0$ correction and they both deliver visually similar images. On the other hand, FSR is able to correct images faster than MFI. Therefore, this chapter will illustrate the use of FSR on images taken from the low-field scanner. To this end, three datasets will be used; a tube phantom, and two brain scans where one has stronger $\triangle B_0$ inhomogeneity than the other. Unfortunately, the current datasets only cover B_0 inhomogeneity, therefore the correction of gradient non-linearity is not shown.

5.1. Tube Phantom

The tube phantom consists of a set of 45 equally-spaced tubes in a rectangular grid filled with sunflower oil, shown in Figure 5.1. It was taken with an FOV of $224 \times 224 \times 200$ mm^3 and time shift of $150\mu s$. As explained in Section. 3.1, two scans are done on the phantom with varying echo times, and is subsequently passed through a 3D sine bell squared filter to reduce noise in the data. The image is then reconstructed using FFT and is shown in Figure 5.2a.

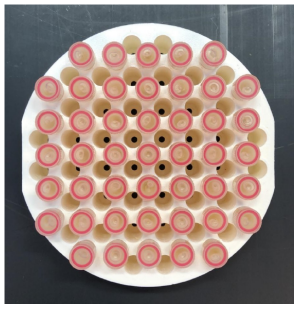

Figure 5.1: Top view of tube phantom showing 45 equally-spaced tubes in a rectangular grid filled with sunflower oil

Subsequently, the phase difference between the two images is used to estimate the $\triangle B_0$ field map using Equation 3.1. Then, it is fitted to a basis of second-order spherical harmonics. These are shown in Figure 5.2b and 5.2c respectively.

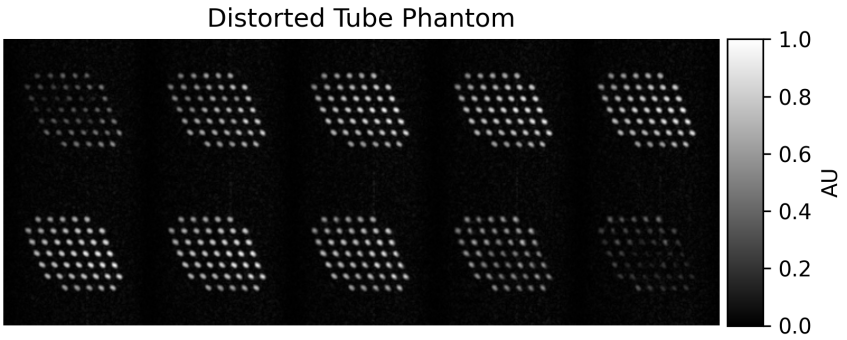

(a) Tube phantom distorted due to $\triangle B_0$ inhomogeneity.

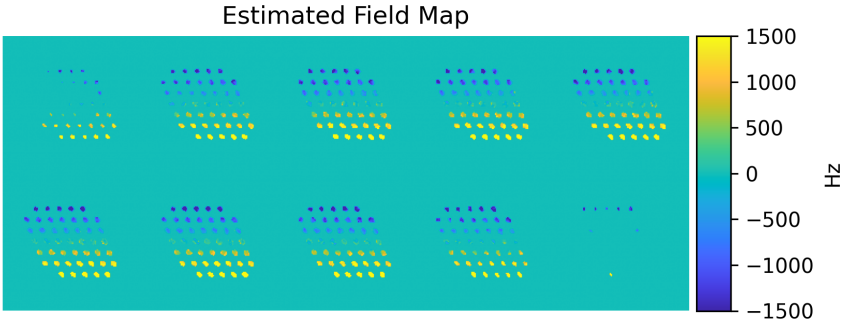

(b) Estimated field map

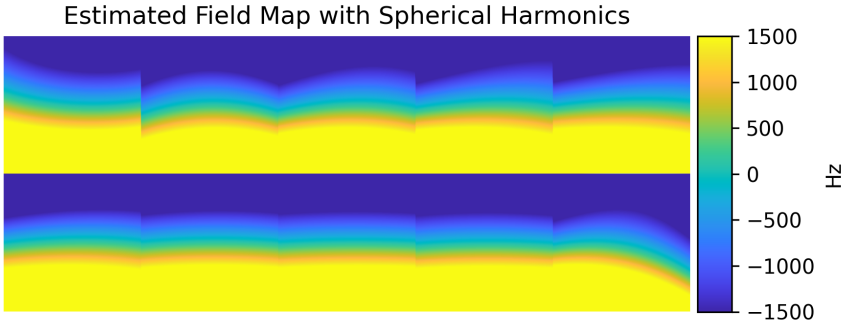

(c) Estimated field map with spherical harmonics

Figure 5.2: **a** Initial distorted tube phantom after the 3D sine bell squared filter. **b** Estimated field map of the image. **c** Estimated field map fitted to a basis of second-order spherical harmonics to span the whole FOV.

Finally, FSR is used with the $\triangle B_0$ field map to obtain a corrected image as shown in Figure 5.3. The FSR step takes 11.4s.

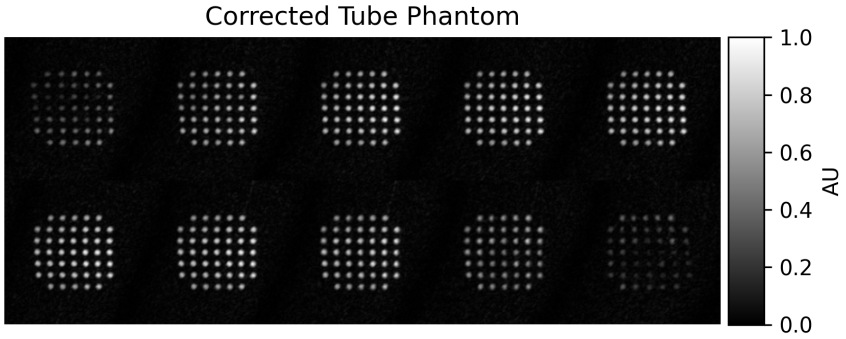

Figure 5.3: Resulting FSR corrected images of the tube phantom.

5.2. BRAIN SCAN

Two in vivo brain datasets were obtained with an FOV of $224 \times 224 \times 200$ mm^3 and a time shift of $150\mu s$. The B_0 field inhomogeneity is stronger in the second dataset, resulting in a more distorted image. This was done by attaching an external magnet to the Faraday cage (Koolstra et al., 2021).

Similar to the last section, each dataset contains two sets of images taken with a time shift. This allows the estimated field map to be obtained, and subsequently, spherical harmonics was used so that the field map spans the whole FOV. Then, FSR was used to correct the images, as shown in Figure 5.4 and 5.5 where the original image is reconstructed using FFT and shown for comparison. It took 14.3s to correct for the dataset with weak B_0 inhomogeneity, and 37s for the dataset with strong B_0 inhomogeneity.

Visually, FSR is able to correct both datasets, although it is hard to gauge how well it was corrected. Supposing that the weak B_0 field distorted dataset was corrected better than the strong B_0 field distorted dataset, comparing the two results in a residual norm error of 0.325. Which means that the strong B_0 field distorted dataset was not corrected as well as its weaker counterpart. Moreover, in both datasets, slice 17 onwards show an indentation and a bright spot in the bottom right of the image that cannot be corrected, this artefact is likely caused by non-linear gradient fields in the scanner, and therefore, could not be accounted for due to a lack of data.

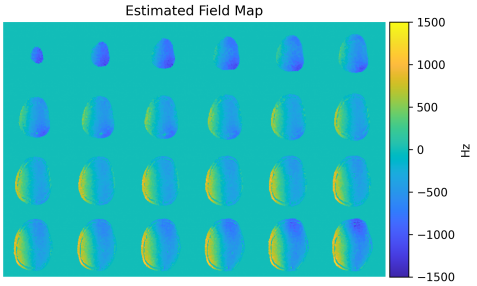

(a) Estimated field map.

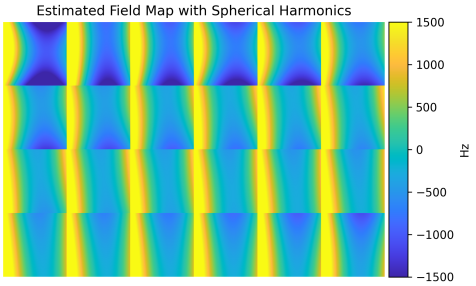

(b) Estimated field map with spherical harmonics.

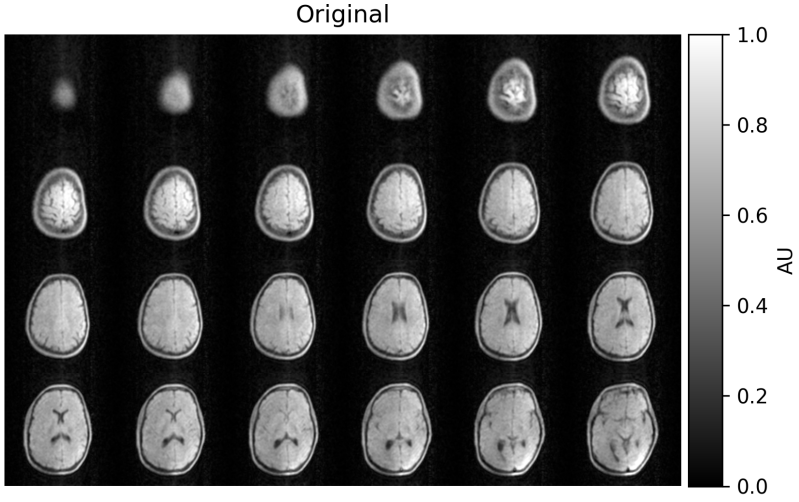

(c) Original in vivo brain images with weak B_0 field inhomogeneity

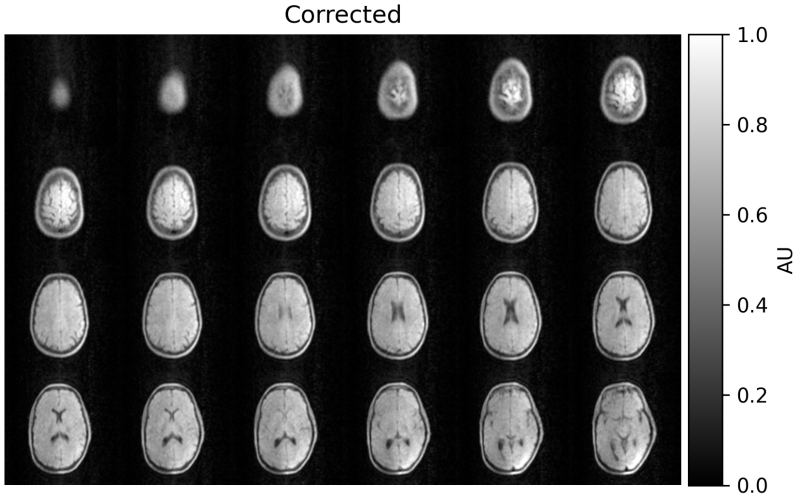

(d) FSR corrected in vivo brain images with weak B_0 field inhomogeneity

Figure 5.4: Weak B_0 inhomogeneity **a**. Estimated field map taken from two scans with a time shift **b**. Estimated field map fitted to a basis of second-order spherical harmonics, creating a $\triangle B_0$ field map that spans the whole FOV. **c**. Original distorted images of in vivo brain images with weak B_0 field inhomogeneity **d**. FSR corrected images

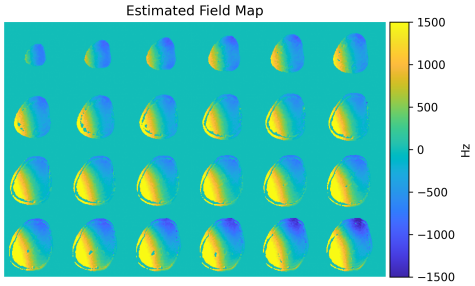

(a) Estimated field map.

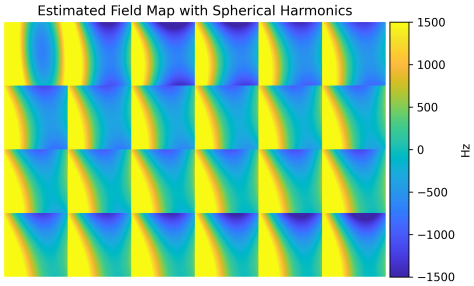

(b) Estimated field map with spherical harmonics.

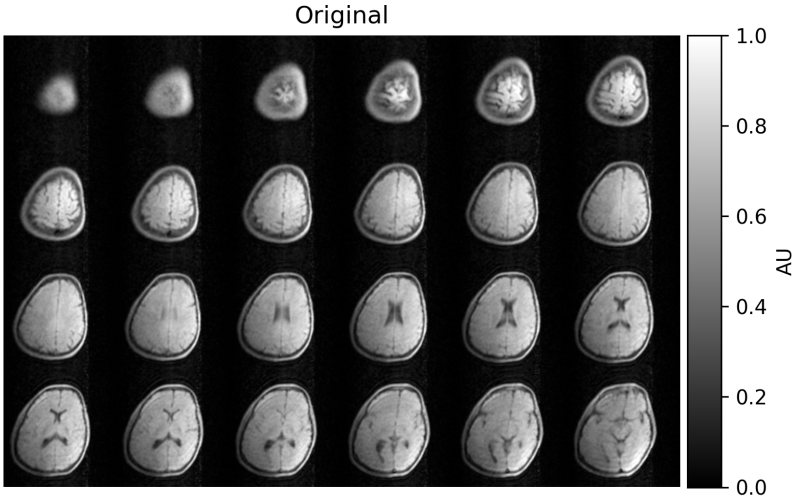

(c) Original in vivo brain images with strong B_0 field inhomogeneity

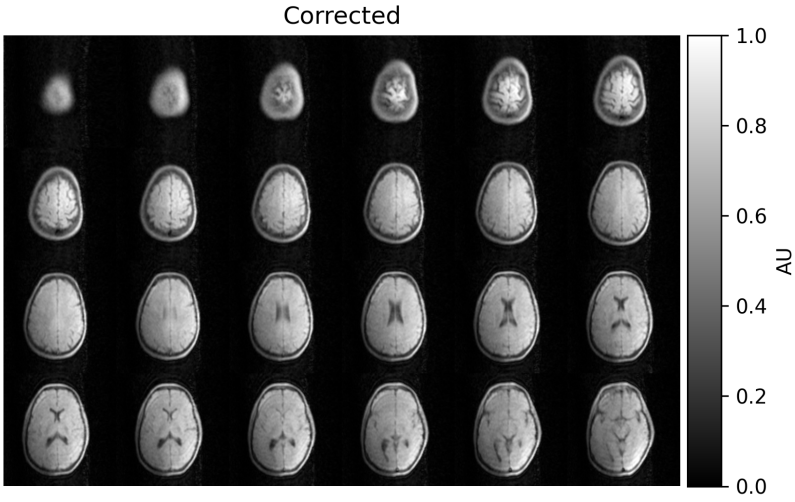

(d) FSR corrected in vivo brain images with strong B_0 field inhomogeneity

Figure 5.5: Strong B_0 inhomogeneity **a**. Estimated field map taken from two scans with a time shift **b**. Estimated field map fitted to a basis of second-order spherical harmonics, creating a $\triangle B_0$ field map that spans the whole FOV. **c**. Original distorted images of in vivo brain images with strong B_0 field inhomogeneity showing more severe distortion. **d**. FSR corrected images

6

Discussion & Conclusion

Firstly, two simulations were done on a $128 \times 128 \times 30$ voxels Shepp-Logan phantom. The first simulation distorts the phantom with B_0 field inhomogeneity, while the second simulation distorts the phantom with both B_0 field inhomogeneity and non-linear gradient fields. To fix the distorted image, three reconstruction techniques were used, full CPR, FSR, and MFI.

The full CPR method acts as a benchmark and shows the limits of the CPR method. As expected, this method takes the longest amount of time, but nevertheless, it gives the best residual norm error that is used as a point of reference for the other methods. FSR was the first optimisation of CPR, and this was done by dividing the range of off-resonance frequencies into segments that limit the accumulation of phase error in each segment to $\frac{\pi}{2}$. By doing this, significantly less images need to be reconstructed to create the corrected image, thereby reducing the duration of reconstruction. The third method used was MFI, which uses even less frequency segments than FSR. To make up for this, coefficients needed to be calculated by using least squares.

Overall, all three methods result in visually similar images of a corrected Shepp-Logan phantom. Looking at the residual norm error of each method shows FSR and MFI staying consistent with full CPR for the B_0 field distorted phantom. When looking at the B_0 and gradient field distorted phantom however, FSR results in a residual norm error increase of 0.002 compared to full CPR and MFI. This shows the efficacy of using the MFI coefficients which is able to stay consistent with full CPR, but nevertheless, no significant improvement was seen when using a higher number of frequency segments combined with the MFI coefficients, and the error stays the same at 0.430. On the other hand, iterative CPR was also tried. To do this, a new field map is estimated subsequently after each iteration of CPR, and this field map is used in the following iteration. But, subsequent iterations result in an increase in error in the estimated field map, likely due to the sensitivity of the estimated field map to noise. Therefore, consecutive iterations result in more distortion instead. Although this was the case in this implementation, Koolstra et al., 2021 shows that iterative CPR is able to improve $\triangle B_0$ error by using Tikhonov regularisation in the estimated field map. This can be implemented in a future iteration of

the project.

In regards to speed, MFI was expected to be the fastest method due to using the least amount of frequency segments. Nevertheless, this was not the case, because calculating the MFI coefficients using least squares unfortunately add to the duration of the method. Using the conjugate gradient least-squares function from Scipy reduces the reconstruction from 2 hours, for correcting the $\triangle B_0$ and gradient field distorted phantom, to 9 minutes while maintaining the same image and residual error. Further optimisation by rounding $\triangle w$ to 1 decimal place is able to reduce the duration of the method to around 3 minutes without an increase in the residual norm error. Nevertheless, this is still longer than FSR, and calculating the MFI coefficients using least squares takes around 90% of the duration of reconstruction. Another method suggested by Man et al., 1997 is to calculate the MFI coefficients by DFT approximation instead of least-squares, this is a possible route to improve the speed of the MFI method and will most likely outperform FSR in both $\triangle B_0$ and $\triangle B_0$ + gradient non-linearity correction.

The in vivo dataset presented contain only B_0 field inhomogeneity, and therefore FSR was used as it provides the fastest reconstruction and has the same residual norm error as the other methods. As explained in Section. 3.1, two scans of each dataset was performed with varying echo times. This was done so that the $\triangle B_0$ field map can be estimated and subsequently expanded to cover the whole FOV using spherical harmonics. Looking at the results of the tube phantom, FSR was able to correct the images sufficiently. Meanwhile, the in vivo brain images show that FSR behaves less favourably when dealt with stronger B_0 field inhomogeneity.

While full CPR takes a very long time, both FSR and MFI result in almost identical corrected images while significantly reducing the amount of time it takes, from hours to minutes. Looking at the correction of $\triangle B_0$ inhomogeneity distortion, FSR and MFI provides similar results with both having the same residual norm error as full CPR, and takes 34.9s and 2m 56.2s respectively. On the other hand, FSR shows an increase in error of 0.002 when correcting for both $\triangle B_0$ inhomogeneity and gradient non-linearity distortion. Therefore, in this case, MFI would be the preferred method because it still gives the same residual norm error as full CPR despite the 62% increase in duration when compared to FSR. Although MFI is slower than FSR at the moment, it is still only a fraction of the time required when compared to full CPR and provides the most consistently accurate correction. Therefore, MFI is recommended for use in future work. In conclusion, both FSR and MFI provide a fast and effective method in correcting for field map inhomogenity, although MFI provide higher accuracy when gradient non-linearity is present.

BIBLIOGRAPHY

Borden, A. E., Dowding, B., Gooderham, E. L., Graham, B., Franklin, W., bo, J., & Szkolny, M. A. (1918). *Hydrocephalus facts*. https://www.geni.com/projects/Hydrocephalus/49669

Börnert, P., Schomberg, H., Aldefeld, B., & Groen, J. (1999). *Magnetic resonance materials in physics*. www.elsevier.com/locate/magma

de Leeuw den Bouter, M. L., van Gijzen, M. B., & Remis, R. F. (2019). Conjugate gradient variants for p -regularized image reconstruction in low-field mri. *SN Applied Sciences*, *1*. https://doi.org/10.1007/s42452-019-1670-2

Dewan, M. C., Rattani, A., Mekary, R., Glancz, L. J., Yunusa, I., Baticulon, R. E., Fieggen, G., Wellons, J. C., Park, K. B., & Warf, B. C. (2019). *Global hydrocephalus epidemiology and incidence: Systematic review and meta-analysis*. https://doi.org/10.3171/2017.10.JNS17439

Dinçer, A., & Özek, M. M. (2011). Radiologic evaluation of pediatric hydrocephalus. *Child's Nervous System*, *27*, 1543–1562. https://doi.org/10.1007/s00381-011-1559-x

Hydrocephalus fact sheet. (n.d.). https://www.ninds.nih.gov/Disorders/Patient-Caregiver-Education/Fac...

Hydrocephalus overview. (n.d.). https://www.mayoclinic.org/diseases-conditions/hydrocephalus/sympt...

Koolstra, K., O'Reilly, T., Börnert, P., & Webb, A. (2021). Image distortion correction for mri in low field permanent magnet systems with strong b0 inhomogeneity and gradient field nonlinearities. *Magnetic Resonance Materials in Physics, Biology and Medicine*, *34*, 631–642. https://doi.org/10.1007/s10334-021-00907-2

Liang, Z.-P., & Lauterbur, P. C. (2000). *Principles of magnetic resonance imaging : A signal processing perspective*. SPIE Optical Engineering Press.

Maeda, A., Sano, K., & Yokoyama, T. (1988). Reconstruction by weighted correlation for mri with time-varying gradients. *IEEE Transactions on Medical Imaging*, *7*, 26–31. https://doi.org/10.1109/42.3926

Man, L.-C., Pauly, J. M., & Macovski, A. (1997). *Multifrequency interpolation for fast off-resonance correction*.

Noll, D. C. (1991). *Reconstruction techniques for magnetic resonance imaging* (Doctoral dissertation). Stanford University.

O'Reilly, T., Teeuwisse, W. M., de Gans, D., Koolstra, K., & Webb, A. G. (2021). In vivo 3d brain and extremity mri at 50 mt using a permanent magnet halbach array. *Magnetic Resonance in Medicine*, *85*, 495–505. https://doi.org/10.1002/mrm.28396

Paladini, D., Malinger, G., Monteagudo, A., Pilu, G., Timor-Tritsch, I., & Toi, A. (2007). *Sonographic examination of the fetal central nervous system: Guidelines for performing the 'basic examination' and the 'fetal neurosonogram'*. https://doi.org/10.1002/uog.3909

Prince, J. L., & Links, J. M. (2015). *Medical imaging signals and systems* (2nd ed.). Pearson Education.

Remis, R. F. (n.d.). *The bloch equation*.

Schabel, M. (2006). 3d shepp-logan phantom. *MATLAB Central File Exchange*, 1–35.

Wald, L. L., McDaniel, P. C., Witzel, T., Stockmann, J. P., & Cooley, C. Z. (2020). *Low-cost and portable mri*. https://doi.org/10.1002/jmri.26942

WorldHealthOrganization. (n.d.). *Global atlas of medical devices*.